

Time-Resolved Potential-Induced Changes in Fe/N/C-Catalysts Studied by In Situ Modulation Excitation X-Ray Absorption Spectroscopy

Kathrin Ebner, Adam H. Clark, Viktoriia A. Saveleva, Grigory Smolentsev, Jingfeng Chen, Lingmei Ni, Jingkun Li, Andrea Zitolo, Frédéric Jaouen, Ulrike I. Kramm, Thomas J. Schmidt, and Juan Herranz*


To advance the widespread implementation of electrochemical energy storage and conversion technologies, the development of inexpensive electrocatalysts is imperative. In this context, Fe/N/C-materials represent a promising alternative to the costly noble metals currently used to catalyze the oxygen reduction reaction (ORR), and also display encouraging activities for the reduction of CO₂. Nevertheless, the application of these materials in commercial devices requires further improvements in their performance and stability that are currently hindered by a lack of understanding of the nature of their active sites and the associated catalytic mechanisms. With this motivation, herein the authors exploit the high sensitivity of modulation excitation X-ray absorption spectroscopy toward species undergoing potential-induced changes to elucidate the operando local geometry of the active sites in two sorts of Fe/N/C-catalysts. While the ligand environment of a part of both materials' sites appears to change from six-/five- to fourfold coordination upon potential decrease, they differ substantially when it comes to the geometry of the coordination sphere, with the more ORR-active material undergoing more pronounced restructuring. Furthermore, these time-resolved spectroscopic measurements yield unprecedented insights into the kinetics of Fe-based molecular sites' structural reorganization, identifying the oxidation of iron as a rate-limiting process for the less ORR-active catalyst.

1. Introduction

Electrochemical processes are at the very foundation of the energy storage and conversion devices required for the electrification and—if renewable electricity is employed—concomitant decarbonization of the energy sector. Specifically, electrolytic H₂-production (and its subsequent re-electrification in fuel cells) and the CO₂-reduction reaction (CO₂RR) will play a critical role in keeping global warming below 1.5 °C by decreasing CO₂-emissions and utilizing the excess of this greenhouse gas to produce value added chemicals.^[1–4] To make such scenarios cost competitive, though, inexpensive electrocatalysts for the reactions at play in these devices are urgently needed. With this motivation, many efforts are being devoted to the development of platinum group metal (PGM)-free catalysts. Out of these, M/N/C-type materials (whereby “M” corresponds to a period 4 transition metal) currently constitute the best performing O₂ reduction reaction (ORR) catalysts,^[5,6] and are further emerging as a

K. Ebner, A. H. Clark, V. A. Saveleva, G. Smolentsev, J. Chen, T. J. Schmidt, J. Herranz
Paul Scherrer Institut
Forschungsstrasse 111, Villigen 5232, Switzerland
E-mail: juan.herranz@psi.ch

L. Ni, U. I. Kramm
Department of Chemistry and Department of Materials
and Earth Sciences
Technical University of Darmstadt
Otto-Berndt-Strasse 3, 64287 Darmstadt, Germany

 The ORCID identification number(s) for the author(s) of this article can be found under <https://doi.org/10.1002/aenm.202103699>.

© 2022 The Authors. Advanced Energy Materials published by Wiley-VCH GmbH. This is an open access article under the terms of the Creative Commons Attribution License, which permits use, distribution and reproduction in any medium, provided the original work is properly cited.

DOI: 10.1002/aenm.202103699

J. Li, F. Jaouen
ICGM
University of Montpellier
CNRS
ENSCM
Montpellier 34090, France

A. Zitolo
Synchrotron SOLEIL
L'orme des Merisiers
BP 48 Saint Aubin, Gif-sur-Yvette 91192, France

T. J. Schmidt
Laboratory of Physical Chemistry
ETH Zürich
Vladimir-Prelog-Weg 2, Zürich 8093, Switzerland

promising contender in the CO₂RR-field.^[7–9] While these materials' initial catalytic activities for both reactions are certainly encouraging,^[6,8,10,11] further increases of their performance and stability are essential for their successful, wide-spread application.^[12] To improve these crucial properties, a better understanding of their active site(s)' operando structures and reaction mechanisms^[10,13,14] is required in hope that this will result in catalyst synthesis developments leading to an enhancement of these sites' density and/or turnover frequencies. Furthermore, such insights will likely advance the development of mitigation strategies for the degradation mechanisms affecting these M/N/C-catalysts, and that currently constitute the major bottleneck for their commercial viability.^[11,15,16]

For these reasons, a large body of work has focused on elucidating the type of active species responsible for these materials' catalytic properties, as well as their electronic structure and functionality.^[7,10] So far, though, no unambiguous conclusions on these matters have been reached, mainly due to the intrinsic complexity of this task; specifically, the plethora of M/N/C-preparation methods reported in the literature, involving various precursors and one or more heat treatment steps at 600–1100 °C,^[17–19] lead to large, synthesis-specific differences among catalysts' N-doped carbon-matrices and metal speciation.^[20–24] The latter is generally acknowledged to consist of 1) inorganic, M-based (nano)particles such as carbides, oxides, and/or nitrides that are often encapsulated in a (N-doped) carbon shell^[20,25] and have occasionally been related to these materials' ORR-activity;^[10,20,22,26,27] and 2) molecularly dispersed sites in which M is complexed by N-moieties embedded in the carbon matrix (often referred to as MN_xC_y-sites),^[10,28,29] and that have been consistently reported to be both CO₂RR- and ORR-active.^[8,10,13,23,30–33] Regarding the latter sites, ongoing characterization efforts employing Mössbauer,^[20,29,34–38] X-ray absorption,^[8,13,20,33,39–45] and X-ray photoelectron spectroscopies^[13,21,46,47] (MS, XAS, and XPS, respectively) alongside theoretical studies^[48–50] have unveiled the simultaneous presence of several kinds of such MN_xC_y-centers differentiated by their electronic structures and M-coordination environments (e.g., number and nature of the N-ligands, possible presence of additional, axially adsorbed O-species). Additionally, these sites are also believed to display significantly different catalytic activities, possibly due to their disparate response to the operative potential; specifically, a vivid debate is still ongoing^[29,24,51] regarding the effect of electrochemical potential on the sites' structure, oxidation- and/or spin-state, which would in terms severely influence the adsorption energies of reaction intermediates on these active centers^[52] and their corresponding catalytic activity.

Achieving an unambiguous picture of these active site(s) operando properties is highly challenging, not only because each of the abovementioned powerful characterization techniques has its own drawbacks (e.g., limited sensitivity to different MN_xC_y-structures for XAS versus restricted applicability of in situ studies for MS and XPS), but also due to these M/N/C-catalysts' compositional heterogeneity and low M-contents (typically <3 wt%). The latter often poses a limit when it comes to signal intensity, especially for electrochemical in situ measurements requiring suitable electrode loadings (commonly <5 mg_{catalyst} cm⁻², i.e., <0.15 mg_{metal} cm⁻²—a comparatively low sample amount for spectroscopic measurements) to achieve

the high catalyst utilizations needed for reliable spectroscopic results.^[53,54] Most crucially, only a low fraction of these MN_xC_y sites are typically located within the operando-relevant catalyst-electrolyte interface (possibly as little as ≈10–20 %, according to recent nitrate-/cyanide-poisoning and in situ MS measurements^[36,37,55–58]) thus jeopardizing the interpretation of in situ spectroscopic results that are likely to be preponderantly representative of the materials' bulk composition.

To overcome this limitation, in this work we have employed modulation excitation (ME-) XAS for the in situ study of two Fe/N/C-catalysts predominantly featuring FeN_xC_y-sites^[36,59,60] but with substantially different ORR-performances. A thorough analysis of the spectra's pre- and rising-edge features, particularly sensitive to the FeN_xC_y-sites' local geometry and electronic configuration, accompanied by extended X-ray absorption fine structure (EXAFS) analysis unveiled that a fraction of the sites in both catalysts undergo a transition from five-/six- to four-fold coordination upon potential decrease. Fine differences in this geometrical reconfiguration (whereby the catalyst prepared using a metal-organic framework (MOF) withstands a greater loss of symmetry at low potentials) were resolved upon subsequent demodulation of the acquired spectra, which allowed discriminating signals corresponding to species unaffected by the potential stimulus (i.e., not located within the catalyst-electrolyte interface). Furthermore, the high time resolution associated to quick-scanning spectral acquisition^[61] led to novel insights on the kinetics of the potential-dependent redox processes undergone by these catalyst systems, and identified the oxidation of the Fe- sites as the rate limiting step of the less ORR-active catalyst derived from a macrocyclic synthesis approach. These findings regarding the geometric and kinetic properties of the molecular sites in these Fe/N/C-catalysts illustrate that the contribution ME-XAS can make to the study of materials and interfacial processes is of great relevance to the electrocatalysis/-chemistry fields.^[62–65]

2. Results and Discussion

The two catalysts included in this study are synthesized following previously reported methods based on Fe-porphyrin versus MOF precursors, for DW21 versus Fe0.5, respectively (see Experimental Section for details). Additionally, both samples have been thoroughly characterized in our recent work,^[59,60] in which ex situ, room temperature MS, and EXAFS spectroscopy showed that their Fe-speciation predominantly consists of FeN_xC_y sites. Specifically, the catalysts' MS spectra (see Figure S1a,b, Supporting Information, and fitting parameters in Table S1, Supporting Information) can be fitted with three doublets, each assigned to a kind of molecular FeN_xC_y site. While the so-called D1 doublet constitutes the preponderant component in both spectra, DW21 features a larger content of the two other doublets (D2 and D3; cf. Figure S1c, Supporting Information). Moreover, even if the complete absence of Fe-based nanoparticles cannot be excluded on the basis of such room temperature MS results,^[24] the lack of Fe-Fe-scattering contributions in the ex situ EXAFS spectra of the catalysts (expected to appear at a phase uncorrected distance of ≈2.2 Å—see Figure S2, Supporting Information) supports

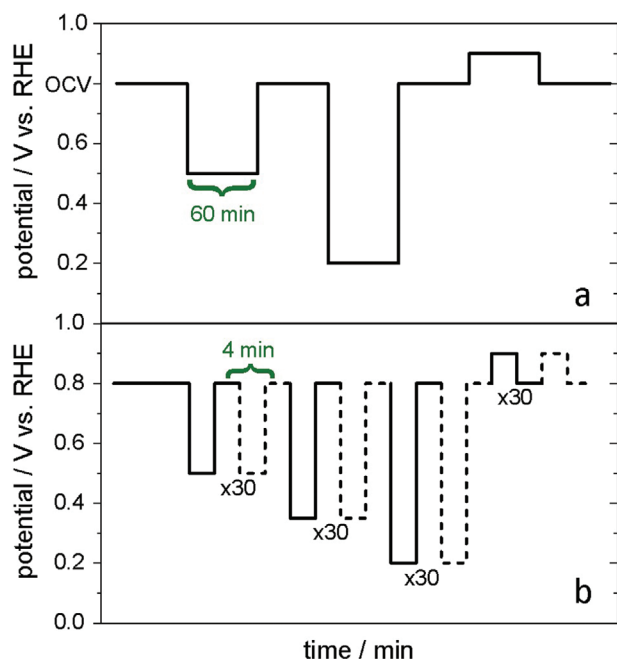


Figure 1. Potential profiles used in the a) standard, step-scan XAS measurements and in the b) quick-scanning ME-XAS experiments. In the latter, each modulation event consisted of 30 switches between a 2 min hold at 0.8 V and a hold of similar length at a vertex potential U_{vertex} .

that the studied catalysts primarily feature molecular FeN_xC_y -sites. Notably, these fine compositional differences are also likely responsible for the distinct differences in ORR activity displayed by the two materials (kinetic current densities at 0.8 V of 0.1 versus 4.1 $\text{A g}_{\text{catalyst}}^{-1}$, or 11 versus 273 $\text{A g}_{\text{Fe}}^{-1}$ for DW21 versus Fe0.5, respectively—see Table S2, Supporting Information), and whose origin we intend to clarify herein.

From this point, we proceed to study the materials in situ in N_2 -saturated 0.5 M H_2SO_4 electrolyte following a careful conditioning protocol that led to catalyst layer apparent utilization values (i.e., ratio between the capacitive currents in the in situ cell and in rotating disk electrode configuration)^[54] of $\approx 65\%$ versus $\approx 75\%$ for DW21 versus Fe0.5, respectively (see details in the Experimental Section and Figure S3, Supporting Information). Here we refrain from performing these measurements in O_2 -saturated electrolyte, since previous studies have shown that the potential-induced changes observed in in situ XAS measurements of similar materials are not affected by the electrolyte saturation atmosphere,^[42,43] and the presence of a reactant gas could further complicate the interpretation of the results in this first ME-XAS study of Fe/N/C-catalysts. Additionally, we focus on investigating potentials below and above the value of the redox transition expected for these materials (at $\approx 0.6\text{--}0.7$ V),^[13,42,66] thus examining structural rearrangements within the ORR-relevant potential range.^[13,20,43,44]

To test the general reversibility of the catalyst systems with regards to the potential stimulus—a primary requirement for ME experiments^[67,68]—we first performed a conventional step scan in situ XAS measurement using the potential profile displayed in Figure 1a (cf. Experimental Section). The excellent agreement among the spectra acquired at 0.8 V just after the initial electrochemical conditioning and those recorded at 0.9 V at

the end of the potential protocol (cf. Figure S4, Supporting Information) prove that the potential-spectroscopy response is indeed reversible for both catalysts within the relevant time scale.

With the reversibility of potential modulation confirmed by step-scanning XAS, ME-XAS experiments in quick-scanning mode utilizing fluorescence detection were performed. The stability and reversibility of the catalysts in the course of these measurements are further confirmed by the consistent signal variation in the course of the potential modulations featured by this time-resolved data (cf. Figure S5, Supporting Information). This observation also attests the catalysts' stability in the course of these XAS measurements, indicating no detrimental beam-damage effects; this is further endorsed by the fact that the absorption edge heights (proportional to the catalysts' Fe-content) remained constant, thus demonstrating that Fe-leaching does not occur in the course of the experiments.

Following these important verifications, we start evaluating the results of the quick-scanning experiments (see potential profile in Figure 1b) by considering the so called period-averaged (PA-) data for both catalysts; as discussed in the Experimental Section, these PA-results refer to the spectra acquired from multiple modulation periods between 0.8 V and a vertex potential U_{vertex} , averaging in the time domain the same points from successive modulation periods (considering the reproducible, last 22 cycles) to obtain a PA dataset. These U_{vertex} -dependent, PA spectra are displayed in Figure S6, Supporting Information. Additionally, the spectral responses within each individual potential modulation stimulus were deconvoluted by means of multivariate curve resolution (MCR) analysis yielding two spectral components for each catalyst and potential modulation. Since these spectra can be differentiated based on their lower versus higher absorption edge energies, corresponding to more reduced versus oxidized components, in the following they will be referred to as $\text{MCR}_{\text{reduced}}^{U_{\text{vertex}}}$ and $\text{MCR}_{\text{oxidized}}^{U_{\text{vertex}}}$, respectively. Interestingly, as shown in Figure S6, Supporting Information, the $\text{MCR}_{\text{reduced}}$ spectra at 0.2, 0.35, and 0.5 V excellently match the most reduced PA spectra acquired at the same potentials (and this also extends to the $\text{MCR}_{\text{oxidized}}$ - and PA-spectra acquired at 0.9 V). This strong agreement implies that these MCR spectra are representative of the catalysts' state at the respective U_{vertex} and, since their quality is better than that of the corresponding PA-data, in what follows we base our analysis on these MCR results.

As it can be seen in Figure 2a and Figure S7, Supporting Information (for DW21 versus Fe0.5, respectively), as the value of U_{vertex} decreases (i.e., $U_{\text{vertex}} = 0.5, 0.35, \text{ or } 0.2$ V) the absorption edge position shifts to lower energies. This is indicative of a decrease of the average oxidation state induced by the reductive potential, with a lower U_{vertex} bringing about a higher degree of reduction. To assess this effect quantitatively, we estimated the edge positions of several reference compounds featuring Fe(II) or Fe(III) ions in a N-coordination environment (i.e., resembling the hypothesized structures of the sites in these catalysts),^[19,69] which appear listed in Table S3, Supporting Information (and whose X-ray absorption near edge structure [XANES] spectra are displayed and further discussed below). As shown in Figure 2b, the edge position of the MCR spectra reaches values consistent with those of the Fe(II) components upon decreasing the potential to ≤ 0.5 V, implying an

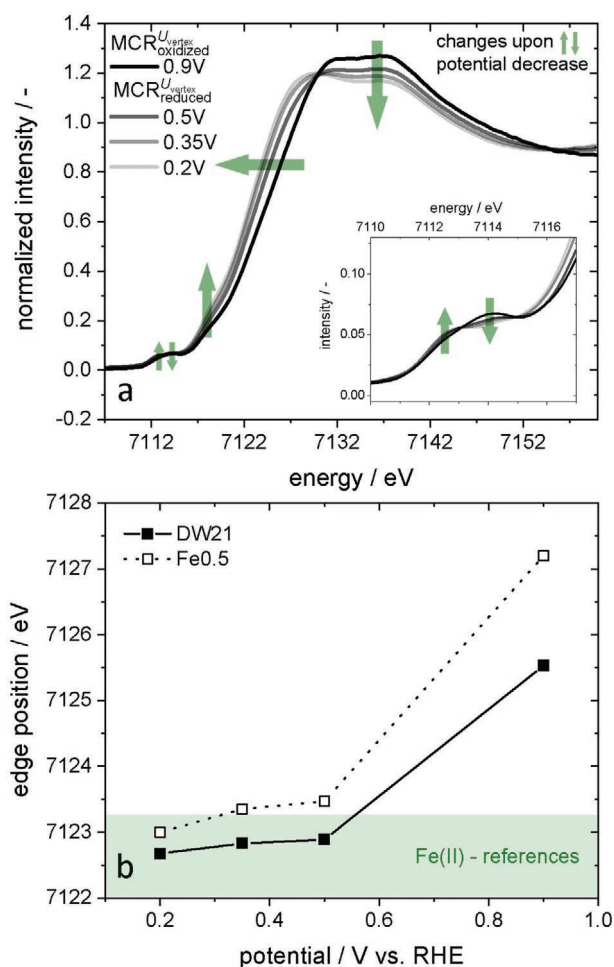


Figure 2. a) DW21's MCR spectra representative of the catalysts' oxidation state in the course of the individual modulation events (i.e., reduced for $U_{\text{vertex}} \leq 0.5$ V, versus oxidized for $U_{\text{vertex}} = 0.9$ V) as a function of the vertex potential. The general spectral changes induced by a decrease of U_{vertex} are indicated with green arrows. b) Effect of U_{vertex} on the spectral edge position, corresponding to the lowest energy maximum in their first derivative. The green shaded area indicates the range of edge positions of various Fe(II)-reference compounds that can be found in Table S3, Supporting Information.

average oxidation state of 2+. Notably, the average oxidation state of DW21 seems to consistently be slightly lower than what is observed for Fe0.5. When the modulation stimulus is performed within the oxidative potential regime (i.e., from 0.8 V to $U_{\text{vertex}} = 0.9$ V) the degree of further oxidation is very mild, as attested by the minimal changes in the concentrations of the $\text{MCR}_{\text{reduced}}^{0.9\text{V}}$ and $\text{MCR}_{\text{oxidized}}^{0.9\text{V}}$ components caused by this potential changes, featured in Figure S8, Supporting Information. This finding indicates that the iron is already predominantly in an 3+ oxidation state at 0.8 V, which is in line with the expected potential of the redox couple at around 0.6 to 0.7 V for this class of materials.^[13,70]

Furthermore, the noted changes in the edge position are accompanied by an altered white line intensity, which corresponds to a $1s \rightarrow 4p$ transition and is symptomatic of modifications of the ligand environment.^[71,72] Concurrently, the spectra

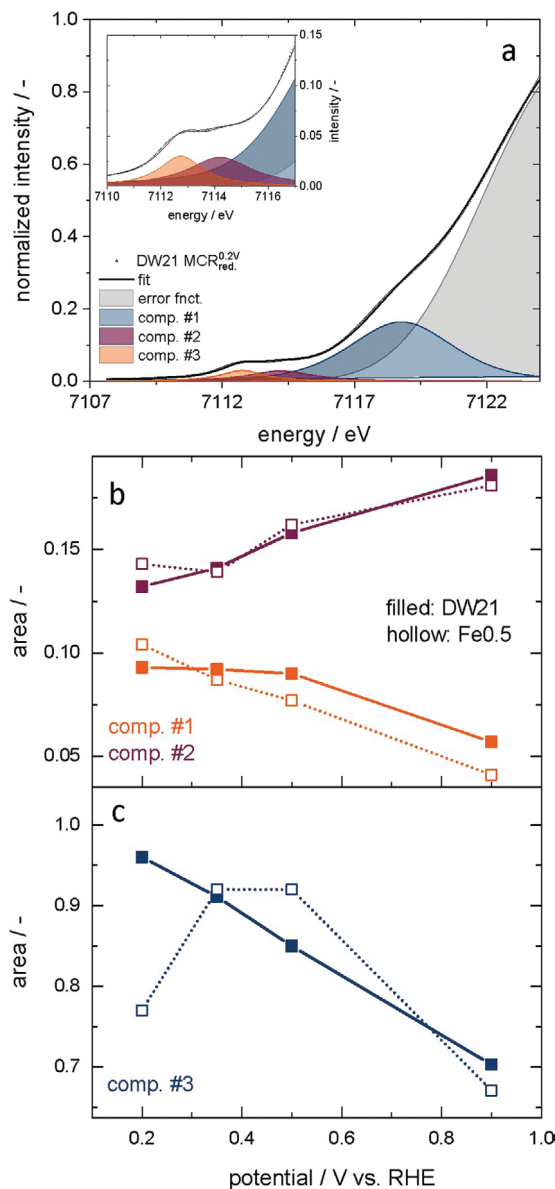


Figure 3. a) Example of a pre-edge fit using three pseudo-Voigt components for the pre- and rising-edge features as well as an error function to model the rising edge of DW21's $\text{MCR}_{\text{reduced}}^{0.2\text{V}}$ spectrum. b) Corresponding effect of U_{vertex} on the intensities of pre-edge components #1 and #2, c) as well as on rising-edge component #3, for each catalysts' $\text{MCR}_{\text{reduced}}$ components at potentials of 0.2, 0.35, or 0.5 V, and for their corresponding $\text{MCR}_{\text{oxidized}}$ components at 0.9 V. Note that all lines are mere guides for the eye.

also feature significant changes in the pre- and rising-edge features (at ≈ 7112 – 7114 and ≈ 7119 eV) that are highly sensitive to the analyte's local geometry and electronic structure, and particularly stem from $1s \rightarrow 3d$ and $1s \rightarrow 4p_z$ electron transitions, respectively.

To quantitatively assess the differences in these pre- and rising-edge features, peak fitting was performed with three pseudo-Voigt profiles and an error-function to simulate the atomic absorption. An example of the resulting fits is shown in Figure 3a, while all other fitted spectra as well as the fitting

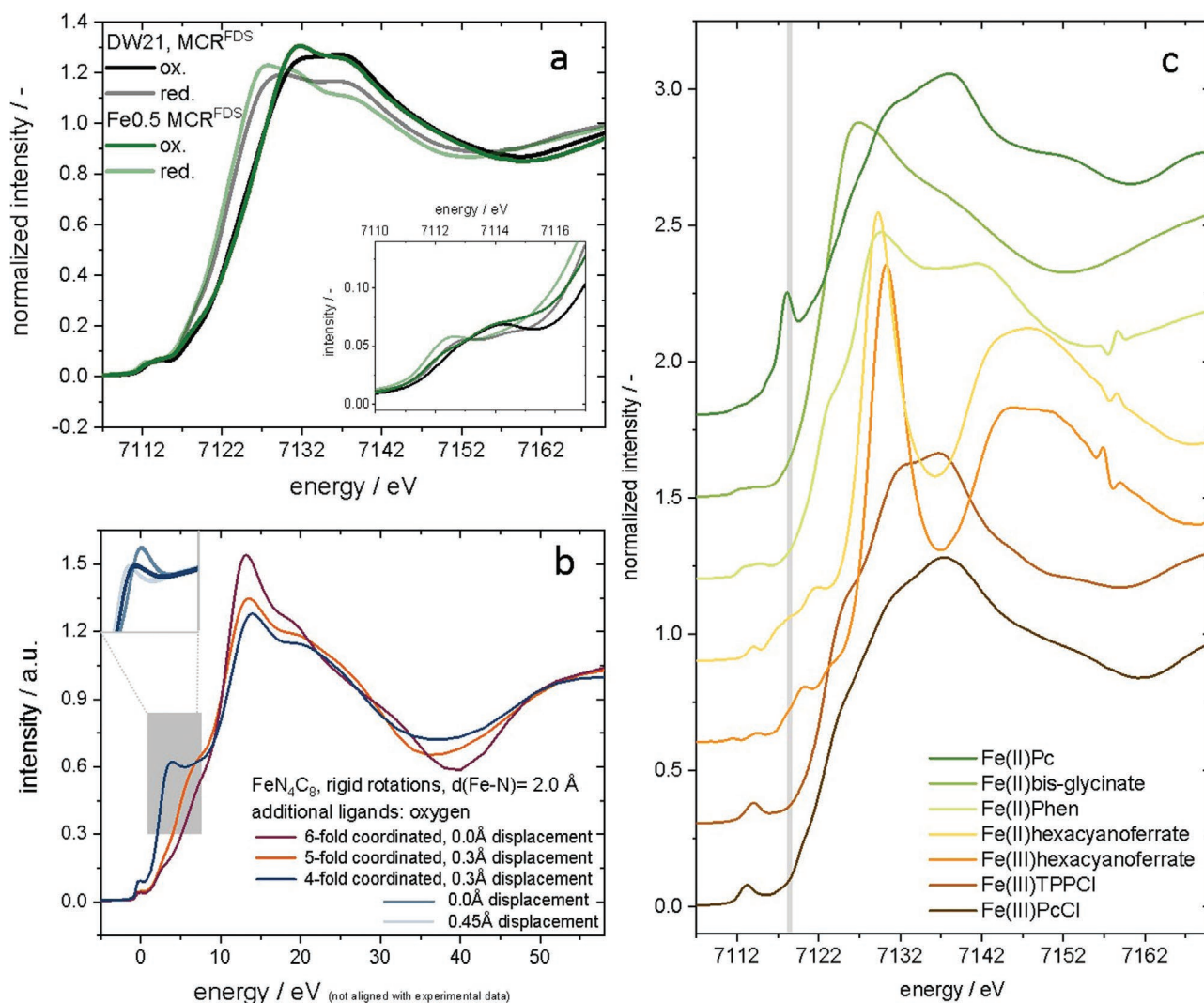


Figure 4. a) Oxidized and reduced MCR components derived from the MCR analysis of the full data sets' PA spectra (MCR^{FDS}) for both catalysts, whereby the pre-edge region appears magnified in the inset. b) Modeled spectra for an FeN₄C₈ unit in six-, five-, or fourfold coordination obtained via FDMNES calculations (rigid rotations, Fe–N-distance = 2.0 Å), whereby the inset shows calculated spectra of the latter unit with different out-of-plane displacements of the central atom. c) XANES of the reference compounds employed in this study, whereby the grey line indicates the energy of component #3 (≈7119 eV). Note that the energy scale in (b) is not aligned with that of the experimental data in (a) and (c).

parameters and constrains can be found in Table S4 and Figure S9, Supporting Information. It should be noted that calculations of pre-edge transitions are nontrivial even for pure compounds,^[73,74] and were not attempted in this study due to the greater complexity brought upon by the intrinsic heterogeneity of these catalysts. Therefore, a tentative assignment of these features based on the comparison with literature and the spectral features of our reference compounds (see Figure S10, Supporting Information) is presented herein. The lower energy pre-edge component (#1, centered at ≈7112.6 eV) is common in Fe(II) compounds,^[74,75] and its relative content increases with a lower vertex potential, as shown in Figure 3b. This increase is accompanied by a concomitant decline in the concentration of the component at ≈7114.2 eV (#2, see Figure 3b), which could be comprised of electron transition contributions from fourfold Fe(II) and/or Fe(III) in fivefold square-pyramidal and/or sixfold octahedral coordinated environments.^[74–76] Furthermore, based on the relatively small intensity

of these pre-edge features, the presence of significant amounts of tetrahedrally coordinated Fe-centers (i.e., devoid of centro-symmetry, and leading to characteristically intense pre-edges), can be excluded.^[75,77] Interestingly, within the error associated to this spectral deconvolution, the magnitude of the changes in these pre-edge features is similar for both catalysts and occurs linearly over the vertex potential range.

Complementarily, the rising edge shoulder at ≈7119 eV (component #3, Figure 3c) is characteristic of a transition in centro-symmetric square-planar Fe(II)-components,^[13,71,74,75] as attested by the exclusive presence of this feature in the spectrum of Fe(II)-phthalocyanine, featured in Figure S10, Supporting Information, and **Figure 4c**. This feature's intensity increases upon lowering U_{vertex} down to 0.5 V for both catalysts, indicating a potential-driven growth of the relative content of sites with a square-planar (i.e., Fe–N₄) geometry. The latter is consistent with the concomitant boost of the fourfold coordinated

component at the expense of the fivefold or sixfold coordinated ones inferred from the pre-edges' analysis discussed above. On the other hand, the intensity of the rising-edge shoulder sharply drops for the Fe_{0.5} sample when a vertex potential of 0.2 V is reached, indicating a loss of D_{4h} symmetry that has been linked to molecular sites with their central atom significantly out-of-plane.^[42,78] Considering the much higher activity of this catalyst, this structural difference may be of high relevance for catalytic performance. Notably, a quantitative analysis of the pre- and rising-edge features for the spectra acquired in step-scan mode leads to the same trends described herein (cf. Figure S11, Supporting Information), further confirming these results.

Most importantly, the changes in components #1–3 upon potential decrease can be tentatively assigned to a partial transformation from a high potential, fivefold or sixfold coordinated Fe(III) structure to an Fe(II)-center with four ligands at low potential. One must bear in mind, though, that assignments based on this analysis are qualitative, and that the changes inferred by it should be regarded as an “average” of the transformations undergone by the different kinds of sites within these catalysts' heterogeneous interface (i.e., it does not allow differentiating the extent to which these transformations affect each of these potential-sensitive centers).

Following this examination of the MCR components for modulation events with different U_{vertex} potentials, the MCR analysis was extended to the totality of the acquired data (i.e., all PA spectra acquired over the course of the experiment between all applied potentials, illustrated in Figure 1b). This led again to the identification of two significant components in each catalyst, implying that the main spectroscopic features of all spectra acquired per catalyst can be described sufficiently well (lack of fit <0.6%) with only two (sets of) XAS-discernible species that change upon potential modulation. In what follows, we differentiate these MCR components again on the basis of their energy shifts, thus assigning them to a reduced and an oxidized component ($\text{MCR}_{\text{reduced}}^{\text{FDS}}$ versus $\text{MCR}_{\text{oxidized}}^{\text{FDS}}$, where FDS stands for “full data set”). Figure 4a displays the spectra of these MCR^{FDS} components for both catalysts, which generally display resembling features when comparing the oxidized or reduced spectral shapes inferred for each of the catalysts. Notably, the pre- and rising-edge fitting method introduced above was extended to the analysis of these MCR^{FDS} spectra, yielding results that compare very well with those discussed above for $\text{MCR}_{\text{oxidized}}^{0.9\text{V}}$ and $\text{MCR}_{\text{reduced}}^{0.2\text{V}}$ (cf. comparisons in Table S4 and Figure S12, Supporting Information), with only small differences in the intensity of the rising-edge shoulder (i.e., component #3) for the reduced states.

To further elucidate the origin of these spectral features, we employed finite difference method near edge structure (FDMNES) modeling,^[79] which provides ab initio simulations of K-edge XAS spectra. Figure 4b displays the spectrum obtained for an FeN₄C₈ unit in a fourfold square-planar coordination, alongside the spectra of equivalent, fivefold and sixfold coordinated structures including additional oxygen ligands and considering various extents of out-of-plane displacement for the central Fe-atom (specified in the Figure's legend). As it can be seen in the inset, a sharp rising edge feature is observed for any fourfold coordinations independent of the out-of-plane displacement. While one could argue that the absence of this

sharp feature in the experimental spectra excludes the presence of a square-planar site structure in our catalysts, its presence (if attenuated) has been confirmed by the pre-/rising-edge analysis above (cf. comp. #3 in Figure 3), a qualitative comparison to the various reference components employed herein, and the derivative analysis of resembling catalysts reported elsewhere.^[20,41,80] As pointed out in those studies, there are several effects that could lead to such a strong dampening of the rising edge peak. First, the active sites in such catalysts are incorporated in an extended carbon matrix that cannot be encompassed by molecular simulations restricted to such a small model unit, and that alter the electronic properties at the metal atom. This extent is confirmed by the differences observed in the XAS spectra of transition metal macrocycles and their derivatives adsorbed on carbon,^[71,81] as well as by the comparatively less intense rising edge featured by Fe(II)-phthalocyanine (see Figure 4c—peaking at a normalized intensity of ≈ 0.4 , as opposed to ≈ 0.6 for the fourfold coordinated model compounds in Figure 4b). Second, as stated above, such a fourfold coordinated compound may represent only one of several site structures displaying a concerted potential response and consequently be present only in small quantities. This assumption is well in line with the view of Fe/N/C-catalysts being comprised of a plurality of sites, reflected by our MS results (Figure S1, Supporting Information) and commonly agreed upon in the field.

When it comes to the white line (i.e., spectral maxima) features, it should be noted that these are strongly influenced by the ligand environment (angles, bonding distances, etc.) and consequently difficult to accurately simulate without a detailed knowledge of the site structure. As an example of this, Briois et al. showed that a spin transition caused by a reduction of the Fe–N bond length led to a dampening and shift to higher energies of the first white line feature $\approx +12$ eV relative to the adsorption edge, alongside the appearance of another white line shoulder at $\approx +15$ eV.^[82] Similarly, Boillot et al. described a lowering of the absorption intensity and a shift of the edge band to higher energies due to the destabilization of the antibonding levels.^[83] Nevertheless, for the bond length of 2.0 Å considered in these calculations (and based on the EXAFS analysis presented below), increasing the number of ligands causes a rise of the first white line feature. This is consistent with the observations of Marshall-Roth et al. for O-bridged pyridinic hexaazacyclophane macrocycles, in which the Fe-center is surrounded by four in-plane N- and one axial O-atoms.^[84] Notably, this white line feature is also enhanced in the MOF-based catalyst versus the porphyrin-based sample (see Figure 4a), potentially indicating a larger fraction of five- or six-coordinated Fe-based sites in Fe_{0.5} versus DW21.

Up to this point, our study has focused on spectral information representative of the catalysts' complete Fe-speciation, that is, without discriminating the fractions of the results related to sites buried in the samples' bulk or located at the catalytically relevant solid/electrolyte interface. Since the latter species reacting upon potential change and most probably responsible for the samples' ORR-activity only represent a fraction of the catalysts' overall Fe-content, an enhanced sensitivity to these interfacial component(s) becomes of high relevance to better understand their involvement in the catalytic processes. This can be attained

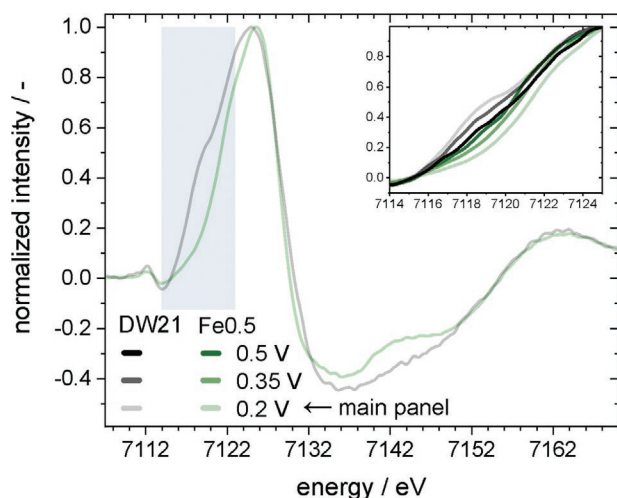


Figure 5. Comparison of normalized PSD amplitudes at a phase angle of 165° for potential modulation events with different U_{vertex} values (indicated in the legend) for both catalysts. The main panel shows data only for $U_{\text{vertex}} = 0.2\text{V}$ for both catalysts. The energy region corresponding to the rising edge (at $\approx 7119\text{ eV}$, cf. component #3 in Figure 3a) is shaded in light blue, magnified in the inset and shown for different U_{vertex} values.

through the phase sensitive detection (PSD) spectra obtained by demodulating the ME-XAS spectra using Equation (2) which, as described above, filters any signals corresponding to noise and/or Fe-based species that do not reversibly respond to the potential stimulus. As a consequence, the signal-to-noise ratio of the resulting, demodulated spectra is greatly enhanced, as illustrated by the comparison between the normalized PSD spectrum in a 0.8/0.2 V modulation event and the significantly noisier difference (sometimes referred to as $\Delta\mu$ spectrum^[85,86]) of the PA spectra at two potentials of the same modulation event (i.e., 0.8 and 0.2 V), see Figure S13, Supporting Information.

When comparing the PSD spectra of the two catalysts resulting from demodulation of the data sets within the different potential modulation events (Figure 5), significant differences between the two samples become more apparent. Particularly focusing on the shoulder related to $1s \rightarrow 4p_z$

electronic transitions arising from D_{4h} symmetry in a square-planar component (corresponding to the XANES' rising edge component #3 at $\approx 7119\text{ eV}$, as discussed above), both catalysts' PSD spectra display similar intensities when considering the 0.8/0.5 V modulation event, indicating a similar coordination of their active species in this potential region. However, the samples react differently to potential switches with lower U_{vertex} values. Specifically, for DW21 this peak's intensity progressively increases for the 0.8/0.35 and 0.8/0.2 V modulation events, while losing intensity for Fe0.5, likely suggesting a different geometry at lower potentials. While more pronounced in the PSD data, these trends agree well with the above results of the spectral rising edge fitting, whereby a progressive increase of centro-symmetry with decreasing potential was inferred for the interfacial sites in the DW21 sample. Concomitantly, in the case of Fe0.5, lowering the potential to 0.2 V leads to a (sharp) drop of the XANES' rising edge component #3 in Figure 3c and of the corresponding intensity of the PSD shoulder at $\approx 7119\text{ eV}$ (Figure 5); this effect is ascribable to a loss of symmetry that could in terms be caused by 1) a decrease in the number of coordinating atoms^[7,44,48,87] (i.e., light scatterers like N, O, and/or C), and/or 2) to the progressive distortion of the coordination sphere by an out-of-plane movement of the Fe-ion, as postulated previously.^[13,20,41]

To shed light on the origins of these differences, we performed a first shell EXAFS analysis of the individual MCR components $\text{MCR}_{\text{reduced}}^{\text{FDS}}$ and $\text{MCR}_{\text{oxidized}}^{\text{FDS}}$. Notably, while the EXAFS cannot fully differentiate local coordination geometries (e.g., tetrahedral versus square-planar), it is a powerful tool to discern the number of and distance to neighboring atoms, as well as their type when the differences in their atomic numbers are sufficiently large. The first shell coordination numbers (N) inferred from these fits of the bulk MCR components' spectra are displayed in Figure 6a, while their R- and k-space spectra are shown in Figure 6b and Figure S14, Supporting Information, and the individual fits and additional derived parameters are depicted and listed in Figure S15 and Table S5, Supporting Information, respectively. The derived N -values for light element scatterers (i.e., O, N, or C) account to ≈ 5 versus ≈ 4 , that is, an average change of one ligand, for both catalysts' oxidized

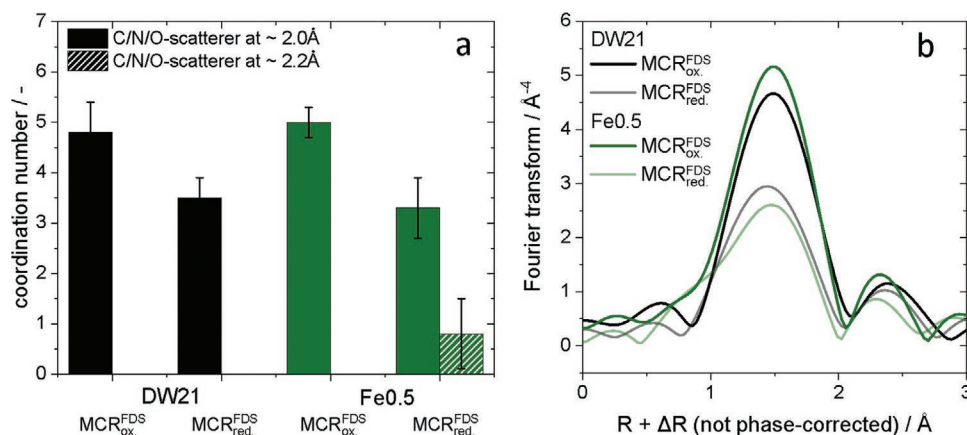


Figure 6. a) Coordination numbers derived from the fitting of the Fourier-transformed EXAFS of both catalysts' $\text{MCR}_{\text{reduced}}^{\text{FDS}}$ and $\text{MCR}_{\text{oxidized}}^{\text{FDS}}$ components and b) corresponding Fourier-transformed EXAFS spectra of both catalysts' $\text{MCR}_{\text{reduced}}^{\text{FDS}}$ and $\text{MCR}_{\text{oxidized}}^{\text{FDS}}$ components showing a decrease in coordination with decreasing potential.

versus reduced MCR components, respectively. This further supports the above interpretation of the XANES features (see Figure 3), which suggested a partial presence of a fourfold coordinated Fe(II)-species in square-planar geometry among the reduced species and a fivefold coordinate Fe(III) in square-pyramidal structure as a likely oxidized component (whereby the symmetry and consequently the extent of planarity in each site have been shown to differ for the two catalysts). Furthermore, these N -values are in agreement with previous studies that proposed that the Fe in these sites is fourfold coordinated by nitrogen plus an additional (O-based) ligand at higher potentials.^[20,42,88] Moreover, the derived bonding distance of ≈ 2.0 Å between Fe and the light scattering elements has been previously assigned to in-plane FeN_4 moieties.^[41,42] It should be noted, though, that the obtained coordination numbers are bulk averages with a significant associated error, as indicated in Figure 6. Therefore, based on these EXAFS-fittings, one cannot claim the exclusive presence of a single site structure, as it is also suggested by MS performed on these catalysts.^[35–37] Interestingly, a high quality fit of the spectrum of the reduced MCR component in the MOF-derived catalyst (i.e., Fe0.5) can only be obtained when including a first shell scatterer at an $\approx 10\%$ larger bonding distance of ≈ 2.2 Å (cf. Figure 6a), possibly indicating that an undetermined fraction of the sites in this reduced condition are geometrically distorted with their Fe significantly out-of-plane.^[41] Alternatively, a fraction of the sites may be undercoordinated, as longer bond distances have been shown for undercoordinated Fe-centers in this type of catalysts.^[44] Specifically, such low (i.e., less than fourfold) coordinated sites have been suggested in previous literature dealing with the use of materials of this class as ORR-^[48,87,89] or CO_2RR -catalysts,^[7,44,90] but it is hard to fathom how such a profound loss of coordination could be reversible (and thus detectable through the ME protocols applied in this work). Therefore, herein we favor the above interpretation that the observed EXAFS changes stem from a displacement of the sites' Fe-ions above their N -coordination plane.

To summarize, in agreement with previous reports^[13,29,41,42,88] our EXAFS analysis suggests a reduction in the number of ligands coordinating the Fe-cation upon potential decrease. This would support the partial presence of a fourfold coordination environment in the reduced state, as derived from the complementary assignment of the pre- and rising-edge features discussed above. The latter, along with the shifts of the edge energy position (Figure 2b), additionally indicate a transition from Fe(III) to Fe(II). Fitting the EXAFS region of Fe0.5 $\text{MCR}_{\text{reduced}}^{\text{FDS}}$ reveals that at a potential of 0.2 V, a fraction of the Fe-based sites in both catalysts is coordinated by light element neighboring atoms at a distance of ≈ 2.2 Å, which we assign to a fourfold coordinated structure with the central Fe significantly out-of-plane. This would qualitatively agree with the reported increase of the Fe–N bond distance previously observed for square-planar compounds with their central Fe-atom out-of-plane, but for which the bonding distance was typically estimated to be ≈ 2.1 Å.^[91,92]

To finalize this study, we take advantage of the high time resolution of the quick-scan ME measurements (2 s—to the best of our knowledge unprecedented for in situ measurements of Fe/N/C-samples with Fe-contents <2 wt%) to shed

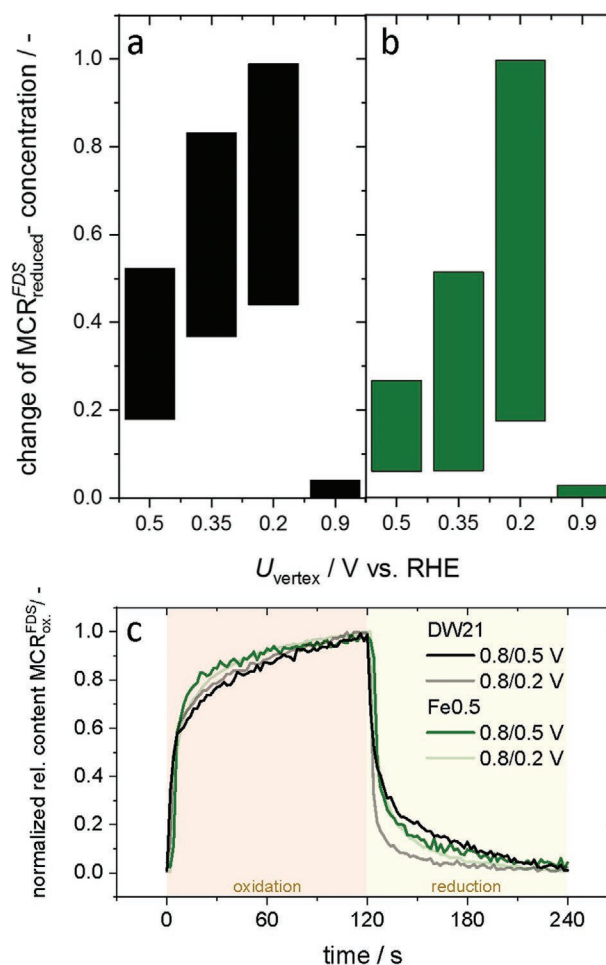


Figure 7. Concentration change of the $\text{MCR}_{\text{reduced}}^{\text{FDS}}$ spectral component obtained from MCR analysis of the entire data set upon potential switches from 0.8 V to U_{vertex} for catalysts a) DW21 and b) Fe0.5, as derived from the spectral-dependent concentration profiles in Figure S16, Supporting Information. c) Concentration profiles of the $\text{MCR}_{\text{oxidized}}^{\text{FDS}}$ component normalized for each modulation, for both catalysts and U_{vertex} values of 0.5 or 0.2 V.

light onto the kinetics of the potential-induced changes in the spectral features as a function of time. From the analysis performed on both catalysts' FDSs (i.e., considering that the latter can be described on the sole basis of one oxidized and one reduced component—see Figure S16, Supporting Information), we infer that—unsurprisingly—employing a more reductive potential in the modulation event results in a higher content of the $\text{MCR}_{\text{reduced}}^{\text{FDS}}$ component. This is better visualized in Figure 7a,b, which summarizes the concentration changes of this $\text{MCR}_{\text{reduced}}^{\text{FDS}}$ spectral component in the course of the potential switches to different U_{vertex} . It becomes evident that the extent of this change is not only potential-, but also catalyst-dependent; specifically, the porphyrin-based, DW21 sample does not appear to return to its initial state at 0.8 V throughout all modulations to reductive potential. In contrast, the MOF-based Fe0.5 sample is capable of attaining this rest state for all modulation events with the exception of the lowest U_{vertex} value (i.e., 0.2 V), indicating that, for a same modulation potential and event duration, the sites in this MOF-based catalyst

features faster transformation kinetics than those in DW21. Additionally, Fe0.5 does not show the gradual increase of the reduced species' content featured by DW21, but rather displays a stark transition when going to the lowest potential (0.2 V) after gradually changing for U_{vertex} values of 0.5 and 0.35 V. This behavior further hints at an additional affinity for such a structural change of the Fe-based sites present in MOF-derived Fe0.5 catalyst, as also indicated by the pre-edge features and EXAFS analyses discussed above.

Complementarily, the individual analysis of each potential modulation event plotted in Figure 7c yields information on the kinetics of the specific transformations of the species involved in each of these potential windows (for a visualization of these results in a logarithmic scale, refer to Figure S17, Supporting Information). Herein we again observe significant differences between the two catalysts: for Fe0.5 the reduction and oxidation processes seem to roughly proceed at the same rates, as inferred from the symmetric shape of the time-profiles for rise and decay of the respective $\text{MCR}_{\text{reduced}}^{U_{\text{vertex}}}$ and the overlay of the concentration profiles for different U_{vertex} values. For DW21, on the other hand, the oxidative process proceeds significantly slower than the reductive counterpart does. These differences are further illustrated in Figure S18, Supporting Information, which displays the time required for two-thirds of the spectral change to occur (i.e., for the content of respective MCR component to increase by 2/3). This facilitates the comparison and demonstrates again the vast rate differences between the oxidation and reduction steps for DW21. Most importantly, these sluggish oxidation kinetics are likely to be the reason why the porphyrin-based DW21 catalyst is not capable of returning to its initial state during each 2 min hold at 0.8 V in the modulation events (cf. Figure 7a).

Moreover, this slow structural rearrangement upon oxidation of the central iron is likely a limiting factor for the adsorption of oxygen-based intermediates on DW21's sites. While these measurements did not implicitly tackle the ORR on these materials, the proposed mechanisms of oxygen adsorption on their sites^[13,42,52] involve a charge transfer from the metal to the O-based ligand that implies the oxidation of the metal center.

As a result, the kinetic sluggishness in the formation of such O-based surface adsorbates inferred herein for DW21 versus Fe0.5 could tentatively explain the ≈ 30 -fold lower O_2 -reduction activity of this porphyrin-based sample when compared to the MOF-derived catalyst (see Table S2, Supporting Information). Interestingly, similar catalyst-dependent differences in the kinetics of surface oxidation and reduction have also been observed in previous time-resolved XAS studies on Pt(-alloy) catalysts for the ORR.^[93,94] Specifically, these Pt-based materials also featured slower kinetics of Pt-oxidation versus reduction and, by analogy with the above discussion, the rates of these surface processes were shown to correlate with their ORR-performance. Thus, future studies including similar time-resolved measurements of a larger number of PGM-free catalysts may allow to verify this hypothetical relation between the kinetics of O-adsorption on FeN_xC_y sites and their corresponding ORR-activity.

Considering the complementary information derived from all the probes employed herein, Figure 8 illustrates our current understanding of the potential-induced changes in geometric properties (and kinetics thereof) undergone by a fraction of the interfacial FeN_xC_y sites in both catalysts. These transitions seem to be comparable for both samples when lowering the potential to 0.5 V, but substantially differ in their character and extent among catalysts at potentials below this value. Specifically, a significant fraction of the interfacial sites in DW21 affected by potential modulation preserve or even enhance their centro-symmetry (Site 1) as the potential decreases, while a fraction of Fe0.5's sites (Site 2) seems to undergo a further restructuring that gives rise to an additional scattering contribution with a longer bonding distance. This difference in the relative contents of both kinds of interfacial sites in each of these two catalysts could be at the origin of the significant ORR-activity differences among them, in agreement with their different Fe-speciation unveiled by other techniques (i.e., MS) with a higher sensitivity than XAS for these fine compositional differences. Furthermore, the rate of the potential-induced redox processes appears to be limited by the slow oxidation of Site 1, particularly evident for the porphyrin-based

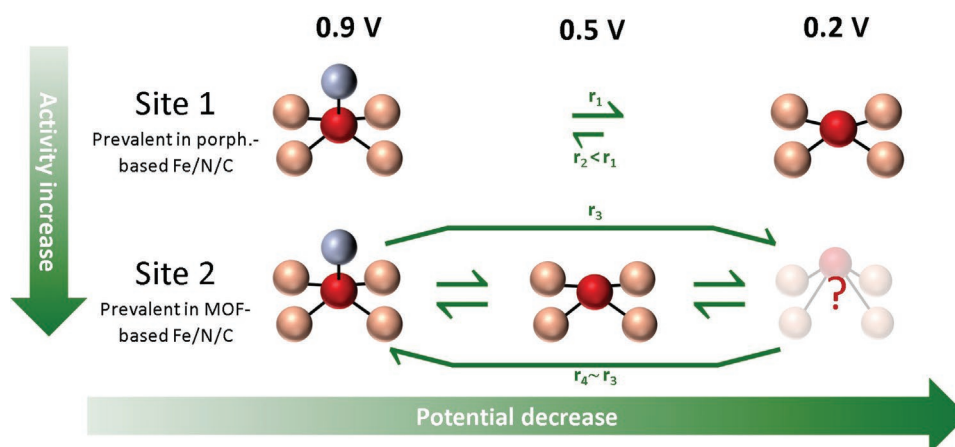


Figure 8. Schematic illustration of the potential-induced structural changes undergone by an interfacial Fe-based species in DW21 (Site 1) and Fe0.5 (Site 2). The shorter arrow indicates a rate limiting process (i.e., slower transformation kinetics). Note that due to both catalysts' heterogeneous Fe-speciation, the simultaneous presence of different structures is expected at each potential.

DW21 sample, whereas the oxidative and reductive processes in Site 2 proceed roughly at the same rate. While at this point we cannot unequivocally discern the reduced structure of Site 2, the data presented herein leads us to speculate that the site is distorted with its central Fe-atom significantly out-of-plane.^[13,41,42] Thus, considering that Site 2 is likely to be the more active site in these materials, further experimental and theoretical work should be devoted to discern its potential-dependent geometrical and electronic properties.

3. Conclusion and Outlook

In conclusion, the data presented herein provides experimental evidence of the different structural changes upon decrease of the electrochemical potential experienced by two Fe/N/C-catalysts, one derived from an Fe-porphyrin and the other from a MOF. A part of the interfacial Fe-based sites in the latter, more ORR-active material, undergoes a structural rearrangement from a five- or sixfold to a fourfold coordinated environment at intermediate potentials (≈ 0.5 V), and another subfraction of these sites further restructure when the potential is lowered beyond that point. While the exact nature of this low potential structure could not be precisely resolved, a loss of centro-symmetry and an increase in the average distance to the neighboring atoms are evident. Therefore, we tentatively propose that this restructured, low potential sites (Site 2) are strongly distorted (i.e., with their Fe displaced out of the N-coordinating plane). While our results also indicate a similar behavior at higher potentials for the porphyrin-based material, the centro-symmetry (i.e., planarity) increases in this case at lower potentials (Site 1). Our analysis of these spectral changes as a function of time reveals that the porphyrin-based catalyst undergoes less overall structural changes when switching from 0.8 to ≤ 0.35 V. This redox process is also particularly slow in the oxidation direction for this porphyrin-based catalyst, while for the MOF-based material the rates of oxidation and reduction are equally high. As a slow structural reorganization upon oxidation hinders the adsorption of O-based species that are likely to also act as ORR intermediates, this rate difference could explain the difference in ORR-activity between these two catalysts.

On top of these new insights on the potential dependence of the active sites' local configuration and kinetics, this study also proves the feasibility of time-resolved XAS measurements on this material class with remarkably low transition metal contents (< 3 wt%), while portraying the strong enhancement of the sensitivity toward electrochemically active species granted by these ME experiments. This opens up the route for in-depth kinetic and mechanistic studies in relevant operating environments (e.g., in the presence of O_2 or CO_2) that will lead to unprecedented operando insight on the role of the transition metal and its coordination environment in the catalytic cycle, and help to clarify how these properties are related to these sites' (in)stability.

4. Experimental Section

The following section focuses on the spectroscopic characterization of the materials and provides brief descriptions of catalyst preparation, complementary characterization, and electrochemical measurements.

Further details on the latter subjects can be found in previous publications.^[33,59,60,95,96]

Spectroscopic Characterization: XAS spectra were recorded at the SuperXAS beamline of the Swiss Light Source (Villigen PSI, Switzerland) operated at 400 mA and 2.4 GeV.^[97] A 2.9 T bending magnet provided a polychromatic beam that was first collimated by a Si-coated mirror, subsequently monochromatized by a Si(311)-monochromator, and then focused by a Rh-coated mirror yielding a spot size on the sample of $\approx 1 \times 0.2$ mm². The measurements were carried out at the Fe K-edge in quick-scanning mode with a monochromator oscillation frequency of 1 Hz and monitoring the fluorescence signal with a passivated implanted planar silicon detector (Mirion Technologies).^[61,97] The latter mode was used for the ME measurements presented herein, since it allowed a higher time resolution than the standard step scanning mode.^[98] Energy calibration was done by setting the first derivative maximum of the simultaneously acquired Fe-foil reference spectra to 7112 eV. The foil was recorded in transmission mode using N_2 -filled ionization chambers (1 bar) that were also employed to detect the incident beam intensity.

Ex situ samples of reference compounds were prepared either in pelletized form using cellulose (Sigma-Aldrich) as a diluent or, in the case of air-sensitive compounds, in quartz capillaries wax-sealed in Ar-atmosphere. A full list of reference compounds is provided in Table S3, Supporting Information. The catalysts were either measured ex situ in Kapton capillaries without dilution or in situ in a flow cell designed for XAS measurement.^[99] Details on electrode preparation and conditioning can be found in the Experimental Section and ref. [53]. In situ experiments on both catalysts were performed in N_2 -saturated electrolyte using a flow cell designed in-house for XAS-experiments.^[99] An Ag/AgCl-electrode calibrated versus reversible hydrogen electrode (RHE) served as the reference electrode in the system. Note that all potentials hereafter are implicitly quoted versus the RHE scale. Working and counter electrodes were spray-coated on conductive Kapton substrates, which had a sputtered gold layer on top to decrease sheet-resistance. Inks for preparing the working electrodes were obtained by mixing the catalyst with isopropanol (Sigma-Aldrich, HPLC gradient grade), ultrapure water (in a ratio of 3:7), and Nafion (5%, Sigma-Aldrich) to obtain a solid-to-liquid ratio of 10 mg. Similarly, an ink was prepared from high surface-area carbon (Black Pearls 2000) and spray-coated to yield the counter electrodes. Loadings between 5.1 and 6.8 mg cm⁻² for both—working and counter electrode—were used. Before mounting those electrodes in the cell, they were wetted with a droplet of electrolyte applying under pressure (≈ 400 mbar for DW21 and ≈ 50 mbar for Fe0.5) to facilitate the removal of air trapped in the catalyst layer. After closing the cell and starting the electrolyte flow, the potential was held at 0.3 V in N_2 -saturated environment to reduce any remaining O_2 (≈ 10 min or until the current stabilizes below 0.05 mA). A Biologic SP-300 potentiostat was used to ensure accurate potential control. For further conditioning, the electrode was cycled 20 times between 0.2 and 1.0 V versus RHE at 50 mV s⁻¹ before reducing the scan rate to 5 mV s⁻¹ and recording another two cycles. After this, depending on the spectra-acquisition mode, one of two protocols was started:

- For step-scan XAS-acquisition using a five-element silicon drift fluorescence detector (SGX), the potential was held at open circuit voltage (OCV) (≈ 0.8 V), 0.5, 0.2 V, OCV, 0.9 V, and again OCV in this order in each case recording three spectra at each potential over the course of 1 h (i.e., 20 min per spectral acquisition).
- For quick-scanning XAS used for ME experiments the potential was modified every 2 min in a square-wave manner as indicated in Figure 1b while continuously recording XAS spectra. Specifically, the potential was first held at 0.8 V (close to both catalysts' OCV) and then at the respective vertex potential (U_{vertex}). This process was repeated 30 times each, while continuously recording XAS spectra. The potentials $E_i = 0.5, 0.35, 0.2,$ and 0.9 V were investigated as described.

As electrode loadings were comparatively high for these flow cell measurements, an entirely wetted catalyst layer allowing full electrochemical utilization could not be expected. Since adequate

probes to characterize the electrochemical utilization in M/N/C-catalyst layers were unavailable, an apparent utilization as compared to RDE measurements, for which the utilization was assumed to be high considering the ≈ 1 magnitude smaller electrode loadings and thicknesses, was determined via the relation

$$\text{utilization}_{\text{apparent}} = \left(\frac{\int_{U_1}^{U_2} I_{N_2}(U) dU}{U_2 - U_1} \right)_{\text{Flow Cell}} * \left(\frac{\int_{U_1}^{U_2} I_{N_2}(U) dU}{U_2 - U} \right)_{\text{RDE}}^{-1} * 100 \quad (1)$$

where U_1 and U_2 were the vertex potentials, ν was the scan rate and I_{N_2} was the current in N_2 -saturated electrolyte. Such apparent utilization amounted to 60–80% (cf. Figure S3, Supporting Information). It should be noted, though, that this represented by no means an accurate evaluation of the sites, which could be electrochemically addressed (i.e., wetted surface sites reacting upon potential change). It was merely supposed to serve as a rough estimation of flow cell catalyst layer utilization.

For XAS data treatment, both ProQEXAFS^[100] and the Demeter software package^[101] were used. The data resulting from step-scan mode measurements was energy-calibrated, averaged over the three recorded spectra and normalized. On the other hand, the spectra acquired in quick-scanning mode measurements were first filtered using a third order Butterworth filter, energy-calibrated, interpolated, and then normalized. To improve the signal-to-noise ratio, four spectra were averaged yielding a time-resolution of 2 s. For ME experiments, 30 cycles were recorded for each vertex potential (cf. Figure 1b and the description in the Experimental Section), whereby only the last 22 cycles were considered to ensure a stable, reproducible behavior upon potential change (cf. Figure S5, Supporting Information). The spectra corresponding to the latter cycles were used in the following two ways: 1) all cycles were averaged in the time domain, and the resulting PA data, representative of the mean spectral response to the respective potential switch, were subsequently analyzed (vide infra); and/or 2) the dataset was demodulated according to literature, where it was shown that phase-resolved modulation spectra for a sinusoidal stimulus could be obtained via:^[102]

$$A_{n,i}(\phi_n^{\text{PSD}}) = \frac{2}{T} \int_0^T A_i(t) \cdot \sin(n\omega t + \phi_n^{\text{PSD}}) dt \quad (2)$$

where T was the period length (4 min, in the experiment presented herein), $A_i(t)$ was the response at a spectral position i in the time-domain, $A_{n,i}(\phi_n^{\text{PSD}})$ was the amplitude in the phase-domain, ω was the modulation frequency, ϕ_n^{PSD} was the phase angle, and n was the demodulation order. Taking into account the square-wave stimulus applied in the experiments herein, which could be expressed as a sum of sinusoidal contributions with odd (i.e., $2n-1$) frequencies, Equation (1) modified to^[103,104]

$$A_{2n-1,i}(\phi_{2n-1}^{\text{PSD}}) = \frac{4}{\pi} \cdot \frac{A_i(t)}{2n-1} |G(i(2n-1)\omega)| \cos(\varphi_{2n-1} - \phi_{2n-1}^{\text{PSD}}) \quad (3)$$

where G was the system's transfer function and ϕ the phase delay.^[103,104] The resulting spectra in the phase-domain (often referred to as "phase sensitive detection" (PSD) spectra) only contain contributions from species that change reversibly with the modulation frequency (or harmonics thereof). This feature greatly enhances the technique's sensitivity to such species and further increases the signal-to-noise ratio, since noise does not respond to the potential stimulus.^[104,67,105,106]

The PSD spectra were then converted to the k -space and the amplitude was corrected as previously described by Chiarello et al.^[68] The EXAFS was subsequently Fourier-transformed in a k -range of 2.6 to 8.5 \AA^{-1} employing a k -weight of 3, and then fitted in an R -range of 1–2.8 \AA . The amplitude reduction factor used in the fit was determined

to be 0.82–0.83 from the Fe-foil reference spectra. For the PA data, on the other hand, MCR analysis was employed for breaking down the spectroscopic data sets into contributions of individual components and their corresponding concentration profiles;^[107–109] for this, the component spectra and their contributions were constrained to be non-negative and, for the latter, to sum to unity. It should be noted that each MCR component did not necessarily represent a pure species.^[110] The resulting components' EXAFS were analyzed using the same parameters as described above.

Finally, the XANES spectra pre- and rising-edge features were fitted with pseudo-Voigt profiles for which the fitting parameters can be found in Table S4, Supporting Information.

Computed Spectra: Fe K-edge XANES spectra were calculated with the FDMNES software^[111,112] using a finite difference method. Calculations were performed using a full-potential approach solving the Schrödinger equation on a discrete grid of points with an interpoint distance of 0.2 \AA . A cluster with a radius of 3.4 \AA was used for calculation, which included four N atoms, eight C atoms, and zero, one, or two O atoms for four-, five-, or six-coordinated models, correspondingly. The O atoms were at a distance of 2.0 \AA of the C_4 symmetry axis of the clusters. To analyze the influence of an out-of-plane displacement of the Fe, the four NC_2 units were considered as rigid and with an Fe–N distance of 2.00 \AA and an Fe–C distance of 3.07 \AA ; Fe atom was in the plane of NC_2 units and moved out-of-plane formed by four N atoms. The energy step for these calculations was 0.01 eV in the region of the rising edge in which resonance states could be observed and then was gradually increased to 0.2, 1.0, and 2.0 eV for higher energies where the changes of the spectrum before energy broadening were smooth. Spectral convolution was made by using an arctangent model.

Catalyst Synthesis: DW21 was prepared by homogeneously impregnating the porphyrin FeTMPPCl (5,10,15,20-Tetrakis[4-methoxyphenyl]-21H,23H-porphine iron[III] chloride, TriPorTech, >96%) on P-XP carbon (PentaCarbon GmbH). To do so, the compound was dissolved in tetrahydrofuran (100 mL THF, 140 mg ⁵⁷Fe-enriched FeTMPPCl) and 300 mg of carbon were added, after which the suspension was sonicated for 1 h. Next, the solvent was removed with the help of a rotary evaporator at slight vacuum. After drying this precursor at 80 °C overnight, the powder was subjected to a heat treatment for 30 min each at 300, 500, and 700 °C in N_2 -atmosphere, whereby the heating ramp was set to 300 °C h⁻¹. Subsequent acid washing (0.1 L of 2 M HCl overnight), filtering, washing, and drying yielded the final catalyst.

On the other hand, the synthesis of Fe0.5 involved the pyrolysis of individual precursors, namely Fe(II)acetate (Sigma-Aldrich, 95% purity), phenanthroline (Sigma-Aldrich, >99% purity), and a Zn(II) zeolitic imidazolate framework (ZIF-8, Basolite Z1200, BASF). After drying these precursors overnight, weighed amounts were mixed and ball-milled, whereby 100 zirconia balls (5 mm diameter) and 1 g precursor powder were subjected to 2 h of milling at 400 rpm in a zirconia crucible. The milled powder was then heat treated for 1 h at 1050 °C in Ar atmosphere (flash pyrolysis).

Further Material Characterization: Both catalysts were extensively characterized in previous publications.^[33,59,60] A detailed description of the procedures followed to synthesize both catalysts and test their electrochemical ORR-activity can be found in the Supporting Information. Additional spectroscopic procedures applied to obtain the results presented herein are specified in the following:

Room temperature MS spectra were acquired in transmission mode on 50–100 mg of sample fixed into a PTFE holder (15 mm diameter) with adhesive tape (Tesa) using a 50 mCi Co/Rh-source. The spectra were fitted with Lorentzian-shaped signals using the Recoil software. The fitting parameters are specified in Table S1, Supporting Information, while the spectra are shown in Figure S1, Supporting Information.

Supporting Information

Supporting Information is available from the Wiley Online Library or from the author.

Acknowledgements

Financial support from the Swiss National Science Foundation (SNSF) through the Ambizione Energy grant PZENP2_173632 is greatly acknowledged by K.E., V.A.S., and J.H.. L.N. and U.I.K. thank the German Federal Ministry of Education and Research (BMBF) for financial support via the NanoMatFutur young researcher group Fe-N-C-StRedO (03XP0092). The authors are grateful to the Swiss Light Source's SuperXAS beamline for the use of their facilities and to Eckhard Bill for valuable discussions. The authors further thank Secil Ünsal-Dayanik and Justus Diercks for their support, David Wallace for providing the catalyst DW21, and Prof. Qingying Jia and Prof. Sanjeev Mukerjee for sharing structural files for XANES modeling.

Open access funding provided by ETH-Bereich Forschungsanstalten.

Conflict of Interest

The authors declare no conflict of interest.

Data Availability Statement

The data that support the findings of this study are available from the corresponding author upon reasonable request.

Keywords

CO₂-reduction reaction, electrochemistry, Fe/N/C-Catalysts, in situ spectroscopy, O₂ reduction reaction, platinum group metal-free

Received: November 25, 2021

Revised: February 3, 2022

Published online: February 21, 2022

- [1] S. J. Davis, N. S. Lewis, M. Shaner, S. Aggarwal, D. Arent, I. L. Azevedo, S. M. Benson, T. Bradley, J. Brouwer, Y. M. Chiang, C. T. M. Clack, A. Cohen, S. Doig, J. Edmonds, P. Fennell, C. B. Field, B. Hannegan, B. M. Hodge, M. I. Hoffert, E. Ingersoll, P. Jaramillo, K. S. Lackner, K. J. Mach, M. Mastrandrea, J. Ogden, P. F. Peterson, D. L. Sanchez, D. Sperling, J. Stagner, J. E. Trancik, et al., *Science* **2018**, 360, eaas9793.
- [2] IPCC, 2018: *Global Warming of 1.5°C. An IPCC Special Report on the impacts of global warming of 1.5°C above pre-industrial levels and related global greenhouse gas emission pathways, in the context of strengthening the global response to the threat of climate change, sustainable development, and efforts to eradicate poverty* (Eds: P. Z. V. Masson-Delmotte, H.-O. Pörtner, D. Roberts, J. Skea, P. R. Shukla, A. Pirani, W. Moufouma-Okia, C. Péan, R. Pidcock, S. Connors, J. B. R. Matthews, Y. Chen, X. Zhou, M. I. Gomis, E. Lonnoy, T. Maycock, M. Tignor, T. Waterfield), **2018**.
- [3] World Energy Council, Paul Scherrer Institut, *World Energy Scenarios 2019 – European Regional Perspective*, World Energy Council, London, **2019**.
- [4] B. Pribyl-Kranewitter, A. Beard, C. L. Gijiu, D. Dinculescu, T. J. Schmidt, *Renewable Sustainable Energy Rev.* **2022**, 154, 111807.
- [5] J. K. Dombrovskis, A. E. C. Palmqvist, *Fuel Cells* **2016**, 16, 4.
- [6] M. Shao, Q. Chang, J.-P. Dodelet, R. Chenitz, *Chem. Rev.* **2016**, 116, 3594.
- [7] A. S. Varela, W. Ju, A. Bagger, P. Franco, J. Rossmeisl, P. Strasser, *ACS Catal.* **2019**, 9, 7270.
- [8] J. Li, P. Pršlja, T. Shinagawa, A. J. M. Fernández, F. Krumeich, K. Artyushkova, P. Atanassov, A. Zitolo, Y. Zhou, R. García-Muelas, N. López, J. Pérez-Ramírez, F. Jaouen, *ACS Catal.* **2019**, 9, 10426.
- [9] S. Paul, Y.-L. Kao, L. Ni, R. Ehnert, I. Herrmann-Geppert, R. van de Krol, R. W. Stark, W. Jaegermann, U. I. Kramm, P. Bogdanoff, *ACS Catal.* **2021**, 11, 5850.
- [10] W. Wang, Q. Jia, S. Mukerjee, S. Chen, *ACS Catal.* **2019**, 9, 10126.
- [11] O. Gröger, H. A. Gasteiger, J.-P. Suchsland, *J. Electrochem. Soc.* **2015**, 162, A2605.
- [12] U.S. Department of Energy Fuel Cell Technologies Office, *Multi-Year Research, Development, and Deployment Plan (MYRDD Plan): Section 3.4, Fuel Cell*, **2016**.
- [13] N. Ramaswamy, U. Tylus, Q. Jia, S. Mukerjee, *J. Am. Chem. Soc.* **2013**, 135, 15443.
- [14] J. Herranz, F. Jaouen, M. Lefèvre, U. I. Kramm, E. Proietti, J.-P. Dodelet, P. Bogdanoff, S. Fiechter, I. Abs-Wurmbach, P. Bertrand, T. M. Arruda, S. Mukerjee, *J. Phys. Chem. C* **2011**, 115, 16087.
- [15] Y. Shao, J. P. Dodelet, G. Wu, P. Zelenay, *Adv. Mater.* **2019**, 31, 1807615.
- [16] S. T. Thompson, D. Papageorgopoulos, *Nat. Catal.* **2019**, 2, 558.
- [17] H. Jahnke, M. Schönborn, G. Zimmermann, *Top. Curr. Chem.* **1976**, 61, 133.
- [18] V. S. Bagotzky, M. R. Tarasevich, K. A. Radyushkina, O. A. Levina, S. I. Andrusyova, *J. Power Sources* **1978**, 2, 233.
- [19] J.-P. Dodelet, *Electrocatalysis in Fuel Cells*, Springer, London **2013**, pp. 271–338.
- [20] Q. Jia, N. Ramaswamy, U. Tylus, K. Strickland, J. Li, A. Serov, K. Artyushkova, P. Atanassov, J. Anibal, C. Gumeci, S. C. Barton, M.-T. Sougrati, F. Jaouen, B. Halevi, S. Mukerjee, *Nano Energy* **2016**, 29, 65.
- [21] K. Artyushkova, A. Serov, S. Rojas-Carbonell, P. Atanassov, *J. Phys. Chem. C* **2015**, 119, 25917.
- [22] K. Strickland, E. Miner, Q. Jia, U. Tylus, N. Ramaswamy, W. Liang, M. Sougrati, F. Jaouen, S. Mukerjee, *Nat. Commun.* **2015**, 6, 7343.
- [23] H. T. Chung, D. A. Cullen, D. Higgins, B. T. Sneed, E. F. Holby, K. L. More, P. Zelenay, *Science* **2017**, 357, 479.
- [24] S. Wagner, H. Auerbach, C. E. Tait, I. Martinaiou, S. C. N. Kumar, C. Kübel, I. Sergeev, H.-C. Wille, J. Behrends, J. A. Wolny, V. Schünemann, U. Kramm, *Angew. Chem., Int. Ed.* **2019**, 58, 10486.
- [25] U. I. Kramm, I. Herrmann-Geppert, J. Behrends, K. Lips, S. Fiechter, P. Bogdanoff, *J. Am. Chem. Soc.* **2016**, 138, 635.
- [26] D. Deng, L. Yu, X. Chen, G. Wang, L. Jin, X. Pan, J. Deng, G. Sun, X. Bao, *Angew. Chem. Int. Ed.* **2013**, 52, 371.
- [27] J. H. Kim, Y. J. Sa, H. Y. Jeong, S. H. Joo, *ACS Appl. Mater. Interfaces* **2017**, 9, 9567.
- [28] C. Médard, M. Lefèvre, J. P. Dodelet, F. Jaouen, G. Lindbergh, *Electrochim. Acta* **2006**, 51, 3202.
- [29] U. I. Kramm, J. Herranz, N. Larouche, T. M. Arruda, M. Lefèvre, F. Jaouen, P. Bogdanoff, S. Fiechter, I. Abs-Wurmbach, S. Mukerjee, J.-P. Dodelet, *Phys. Chem. Chem. Phys.* **2012**, 14, 11673.
- [30] T. N. Huan, N. Ranjbar, G. Rousse, M. Sougrati, A. Zitolo, V. Mougél, F. Jaouen, M. Fontecave, *ACS Catal.* **2017**, 7, 1520.
- [31] W. Ju, A. Bagger, G. P. Hao, A. S. Varela, I. Sinev, V. Bon, B. R. Cuenya, S. Kaskel, J. Rossmeisl, P. Strasser, *Nat. Commun.* **2017**, 8, 944.
- [32] F. Pan, H. Zhang, K. Liu, D. Cullen, K. More, M. Wang, Z. Feng, G. Wang, G. Wu, Y. Li, *ACS Catal.* **2018**, 8, 3116.
- [33] A. Zitolo, V. Goellner, V. Armel, M.-T. Sougrati, T. Mineva, L. Stievano, E. Fonda, F. Jaouen, *Nat. Mater.* **2015**, 14, 937.
- [34] A. L. Bouwkamp-Wijnoltz, W. Visscher, J. A. R. Van Veen, E. Boellaard, A. M. Van der Kraan, S. C. Tang, *J. Phys. Chem. B* **2002**, 106, 12993.
- [35] J. Li, M. T. Sougrati, A. Zitolo, J. M. Ablett, I. C. Oğuz, T. Mineva, I. Matanovic, P. Atanassov, Y. Huang, I. Zenyuk, A. Di Cicco, K. Kumar, L. Dubau, F. Maillard, G. Dražić, F. Jaouen, *Nat. Catal.* **2021**, 4, 10.

- [36] L. Ni, P. Theis, S. Paul, R. W. Stark, U. I. Kramm, *Electrochim. Acta* **2021**, 395, 139200.
- [37] L. Ni, C. Gallenkamp, S. Paul, M. Kübler, P. Theis, S. Chhabra, K. Hofmann, E. Bill, A. Schnegg, B. Albert, V. Krewald, U. I. Kramm, *Adv. Energy Sustainability Res.* **2021**, 2, 2000064.
- [38] K. Ebner, L. Ni, V. A. Saveleva, B. P. Le Monnier, A. H. Clark, F. Krumeich, M. Nachttegaal, J. S. Luterbacher, U. I. Kramm, T. J. Schmidt, J. Herranz, *Phys. Chem. Chem. Phys.* **2021**, 23, 9147.
- [39] K. Iwase, K. Ebner, J. S. Diercks, V. A. Saveleva, S. Ünsal, F. Krumeich, T. Harada, I. Honma, S. Nakanishi, K. Kamiya, T. J. Schmidt, J. Herranz, *ACS Appl. Mater. Interfaces* **2021**, 13, 15122.
- [40] U. Tylus, Q. Jia, K. Strickland, N. Ramaswamy, A. Serov, P. Atanassov, S. Mukerjee, *J. Phys. Chem. C* **2014**, 118, 8999.
- [41] Q. Jia, N. Ramaswamy, H. Hafiz, U. Tylus, K. Strickland, G. Wu, B. Barbiellini, A. Bansil, E. F. Holby, P. Zelenay, S. Mukerjee, *ACS Nano* **2015**, 9, 12496.
- [42] J. Li, S. Ghoshal, W. Liang, M. T. Sougrati, F. Jaouen, B. Halevi, S. McKinney, G. McCool, C. Ma, X. Yuan, Z. F. Ma, S. Mukerjee, Q. Jia, *Energy Environ. Sci.* **2016**, 9, 2418.
- [43] A. Zitolo, N. Ranjbar-Sahraie, T. Mineva, J. Li, Q. Jia, S. Stamatina, G. F. Harrington, S. M. Lyth, P. Krtil, S. Mukerjee, E. Fonda, F. Jaouen, *Nat. Commun.* **2017**, 8, 957.
- [44] J. Gu, C. S. Hsu, L. Bai, H. M. Chen, X. Hu, *Science* **2019**, 364, 1091.
- [45] K. Ebner, J. Herranz, V. A. Saveleva, B. Kim, S. Henning, M. Demicheli, F. Krumeich, M. Nachttegaal, T. J. Schmidt, *ACS Appl. Energy Mater.* **2019**, 2, 1469.
- [46] S. Kabir, K. Artyushkova, A. Serov, B. Kiefer, P. Atanassov, *Surf. Interface Anal.* **2016**, 48, 293.
- [47] K. Artyushkova, I. Matanovic, B. Halevi, P. Atanassov, *J. Phys. Chem. C* **2017**, 121, 2836.
- [48] E. F. Holby, G. Wu, P. Zelenay, C. D. Taylor, *J. Phys. Chem. C* **2014**, 118, 14388.
- [49] C. E. Szakacs, M. Lefevre, U. I. Kramm, J.-P. P. Dodelet, F. Vidal, *Phys. Chem. Chem. Phys.* **2014**, 16, 13654.
- [50] E. F. Holby, P. Zelenay, *Nano Energy* **2016**, 29, 54.
- [51] T. Mineva, I. Matanovic, P. Atanassov, M. T. Sougrati, L. Stievano, M. Clémancey, A. Kochem, J. Latour, F. Jaouen, *ACS Catal.* **2019**, 9, 9359.
- [52] J. H. Zagal, F. Bedioui, J.-P. Dodelet, *N4-Macrocyclic Metal Complexes*, Springer, New York **2006**.
- [53] M. Povia, J. Herranz, T. Binninger, M. Nachttegaal, A. Diaz, J. Kohlbrecher, D. F. Abbott, B. J. Kim, T. J. Schmidt, *ACS Catal.* **2018**, 8, 7000.
- [54] M. Povia, D. F. Abbot, J. Herranz, A. Heinritz, D. Lebedev, B. Kim, E. Fabbri, A. Patru, J. Kohlbrecher, R. Schäublin, M. Nachttegaal, C. Coperet, T. J. Schmidt, *Energy Environ. Sci.* **2019**, 12, 3038.
- [55] D. Malko, A. Kucernak, T. Lopes, *Nat. Commun.* **2016**, 7, 13285.
- [56] F. Luo, C. H. Choi, M. J. M. Primbs, W. Ju, N. Leonard, A. Thomas, F. Jaouen, P. Strasser, *ACS Catal.* **2019**, 9, 4841.
- [57] M. Primbs, Y. Sun, A. Roy, D. Malko, A. Mehmood, M.-T. Sougrati, P.-Y. Blanchard, G. Granozzi, T. Kosmala, G. Daniel, P. Atanassov, J. Sharman, C. Durante, A. Kucernak, D. Jones, F. Jaouen, P. Strasser, *Energy Environ. Sci.* **2020**, 13, 2480.
- [58] G. Bae, H. Kim, H. Choi, P. Jeong, D. H. Kim, H. C. Kwon, K.-S. Lee, M. Choi, H.-S. Oh, F. Jaouen, C. H. Choi, *JACS Au* **2021**, 1, 586.
- [59] M. T. Sougrati, V. Goellner, A. K. Schuppert, L. Stievano, F. Jaouen, *Catal. Today* **2016**, 262, 110.
- [60] V. A. Saveleva, K. Ebner, L. Ni, G. Smolentsev, D. Klose, A. Zitolo, E. Marelli, J. Li, M. Medarde, O. V. Safonova, M. Nachttegaal, F. Jaouen, U. I. Kramm, T. J. Schmidt, J. Herranz, *Angew. Chem., Int. Ed.* **2021**, 60, 11707.
- [61] A. H. Clark, P. Steiger, B. Bornmann, S. Hitz, R. Frahm, D. Ferri, M. Nachttegaal, *J. Synchrotron Radiat.* **2020**, 27, 681.
- [62] Y. Zhu, J. Wang, H. Chu, Y.-C. Chu, H. M. Chen, *ACS Energy Lett.* **2020**, 5, 1281.
- [63] K. J. Lee, N. Elgrishi, B. Kandemir, J. L. Dempsey, *Nat. Rev. Chem.* **2017**, 1, 0039.
- [64] C. W. Machan, *Curr. Opin. Electrochem.* **2019**, 15, 42.
- [65] F. Lin, Y. Liu, X. Yu, L. Cheng, A. Singer, O. G. Shpyrko, H. L. Xin, N. Tamura, C. Tian, T.-C. Weng, X.-Q. Yang, Y. S. Meng, D. Nordlund, W. Yang, M. M. Doeff, *Chem. Rev.* **2017**, 117, 13123.
- [66] L. Osmieri, R. K. Ahluwalia, X. Wang, H. T. Chung, X. Yin, A. J. Kropf, J. Park, D. A. Cullen, K. L. More, P. Zelenay, D. J. Myers, K. C. Neyerlin, *Appl. Catal., B* **2019**, 257, 117929.
- [67] D. Ferri, M. A. Newton, M. Nachttegaal, *Top. Catal.* **2011**, 54, 1070.
- [68] G. L. Chiarello, D. Ferri, *Phys. Chem. Chem. Phys.* **2015**, 17, 10579.
- [69] F. Jaouen, in *Non-Noble Metal Fuel Cell Catalysts* (Eds: Z. Chen, J. Dodelet, J. Zhang), Wiley-VCH, Weinheim **2014**, pp. 29–118.
- [70] L. Osmieri, A. H. A. M. Videla, P. Ocón, S. Specchia, *J. Phys. Chem. C* **2017**, 121, 17796.
- [71] M. C. M. Alves, J. P. Dodelet, D. Guay, M. Ladouceur, G. Tourillon, *J. Phys. Chem.* **1992**, 96, 10898.
- [72] P. G. Santori, F. D. Speck, J. Li, A. Zitolo, Q. Jia, S. Mukerjee, S. Cherevko, F. Jaouen, *J. Electrochem. Soc.* **2019**, 166, F3311.
- [73] Y. Joly, D. Cabaret, H. Renevier, C. R. Natoli, *Phys. Rev. Lett.* **1999**, 82, 2398.
- [74] T. E. Westre, P. Kennepohl, J. G. DeWitt, B. Hedman, K. O. Hodgson, E. I. Solomon, *J. Am. Chem. Soc.* **1997**, 119, 6297.
- [75] M. Wilke, F. Farges, P. E. Petit, G. E. Brown, F. Martin, *Am. Mineral.* **2001**, 86, 714.
- [76] K. E. Loeb, T. E. Westre, T. J. Kappock, N. Mitić, E. Glasfeld, J. P. Caradonna, B. Hedman, K. O. Hodgson, E. I. Solomon, *J. Am. Chem. Soc.* **1997**, 119, 1901.
- [77] G. A. Waychunas, G. E. Brown, M. J. Apted, *Phys. Chem. Miner.* **1983**, 10, 1.
- [78] V. Briois, P. Sainctavit, G. J. Long, F. Grandjean, *Inorg. Chem.* **2001**, 40, 912.
- [79] O. Bun'au, A. Y. Ramos, Y. Joly, *Int. Tables Crystallogr.* **2021**, <https://doi.org/10.1107/S1574870720003304>.
- [80] J. Li, L. Jiao, E. Wegener, L. L. Richard, E. Liu, A. Zitolo, M. T. Sougrati, S. Mukerjee, Z. Zhao, Y. Huang, F. Yang, S. Zhong, H. Xu, A. J. Kropf, F. Jaouen, D. J. Myers, Q. Jia, *J. Am. Chem. Soc.* **2020**, 142, 1417.
- [81] S. Kim, T. Ohta, G. Kwag, *Bull. Korean Chem. Soc.* **2000**, 21, 588.
- [82] V. Briois, C. C. d. Moulin, A. M. Flank, P. Sainctavit, C. Brouder, P. Sainctavit, C. Brouder, *J. Am. Chem. Soc.* **1995**, 117, 1019.
- [83] M. L. Boillot, J. Zarembowitch, J. P. Itié, J. P. Itié, A. Polian, E. Bourdet, J. G. Haasnoot, *New J. Chem.* **2002**, 26, 313.
- [84] T. Marshall-Roth, N. J. Libretto, A. T. Wrobel, K. J. Anderton, M. L. Pegis, N. D. Ricke, T. Van Voorhis, J. T. Miller, Y. Surendranath, *Nat. Commun.* **2020**, 11, 5283.
- [85] M. Teliska, W. E. O'Grady, D. E. Ramaker, *J. Phys. Chem. B* **2005**, 109, 8076.
- [86] D. E. Ramaker, C. Roth, in *Polymer Electrolyte Membrane and Direct Methanol Fuel Cell Technology*, Woodhead Publishing Limited, Cambridge, UK **2012**, pp. 120–145.
- [87] S. Kabir, K. Artyushkova, B. Kiefer, P. Atanassov, *Phys. Chem. Chem. Phys.* **2015**, 17, 17785.
- [88] H. Fei, J. Dong, Y. Feng, C. S. Allen, C. Wan, B. Voloskiy, M. Li, Z. Zhao, Y. Wang, H. Sun, P. An, W. Chen, Z. Guo, C. Lee, D. Chen, I. Shakir, M. Liu, T. Hu, Y. Li, A. I. Kirkland, X. Duan, Y. Huang, *Nat. Catal.* **2018**, 1, 63.
- [89] F. Jaouen, S. Marcotte, J. P. Dodelet, G. Lindbergh, *J. Phys. Chem. B* **2003**, 107, 1376.
- [90] N. Leonard, W. Ju, I. Sinev, J. Steinberg, F. Luo, A. S. Varela, B. R. Cuenya, P. Strasser, *Chem. Sci.* **2018**, 9, 5064.
- [91] W. R. Scheidt, C. A. Reed, *Chem. Rev.* **1981**, 81, 543.

- [92] M. Ferrandon, A. J. Kropf, D. J. Myers, K. Artyushkova, U. Kramm, P. Bogdanoff, G. Wu, C. M. Johnston, P. Zelenay, *J. Phys. Chem. C* **2012**, *116*, 16001.
- [93] N. Ishiguro, T. Saida, T. Uruga, S. I. Nagamatsu, O. Sekizawa, K. Nitta, T. Yamamoto, S. I. Ohkoshi, Y. Iwasawa, T. Yokoyama, M. Tada, *ACS Catal.* **2012**, *2*, 1319.
- [94] N. Ishiguro, S. Kityakarn, O. Sekizawa, T. Uruga, T. Sasabe, K. Nagasawa, T. Yokoyama, M. Tada, *J. Phys. Chem. C* **2014**, *118*, 15874.
- [95] U. I. Kramm, I. Abs-Wurmbach, I. Herrmann-Geppert, J. Radnik, S. Fiechter, P. Bogdanoff, *J. Electrochem. Soc.* **2011**, *158*, B69.
- [96] V. Goellner, V. Armel, A. Zitolo, E. Fonda, F. Jaouen, *J. Electrochem. Soc.* **2015**, *162*, H403.
- [97] O. Müller, M. Nachtegaal, J. Just, D. Lützenkirchen-Hecht, R. Frahm, *J. Synchrotron Radiat.* **2016**, *23*, 260.
- [98] D. Scieszka, J. Yun, A. S. Bandarenka, *ACS Appl. Mater. Interfaces* **2017**, *9*, 20213.
- [99] T. Binninger, M. Garganourakis, A. Patru, E. Fabbri, T. J. Schmidt, O. Sereda, *J. Electrochem. Soc.* **2016**, *163*, H906.
- [100] A. H. Clark, J. Imbao, R. Frahm, M. Nachtegaal, *J. Synchrotron Radiat.* **2020**, *27*, 551.
- [101] B. Ravel, M. Newville, *J. Synchrotron Radiat.* **2005**, *12*, 537.
- [102] D. Baurecht, U. P. Fringeli, *Rev. Sci. Instrum.* **2001**, *72*, 3782.
- [103] A. Urakawa, T. Bürgi, A. Baiker, *Chem. Phys.* **2006**, *324*, 653.
- [104] A. Urakawa, T. Bürgi, A. Baiker, *Chem. Eng. Sci.* **2008**, *63*, 4902.
- [105] P. Müller, I. Hermans, *Ind. Eng. Chem. Res.* **2017**, *56*, 1123.
- [106] V. Marchionni, D. Ferri, O. Kröcher, A. Wokaun, *Anal. Chem.* **2017**, *89*, 5801.
- [107] A. De Juan, J. Jaumot, R. Tauler, *Anal. Methods* **2014**, *6*, 4964.
- [108] C. Ruckebusch, L. Blanchet, *Anal. Chim. Acta* **2013**, *765*, 28.
- [109] A. Voronov, A. Urakawa, W. van Beek, N. E. Tsakouris, H. Emerich, M. Rønning, *Anal. Chim. Acta* **2014**, *840*, 20.
- [110] G. Smolentsev, G. Guilera, M. Tromp, S. Pascarelli, A. V. Soldatov, *J. Chem. Phys.* **2009**, *130*, 174508.
- [111] Y. Joly, *Phys. Rev. B* **2001**, *63*, 125120.
- [112] S. A. Guda, A. A. Guda, M. A. Soldatov, K. A. Lomachenko, A. L. Bugaev, C. Lamberti, W. Gawelda, C. Bressler, G. Smolentsev, A. V. Soldatov, Y. Joly, *J. Chem. Theory Comput.* **2015**, *11*, 4512.